Multiscale estimation of GPS velocity fields

Carl Tape, Pablo Musé, Mark Simons

Seismological Laboratory, California Institute of Technology, Pasadena, California 91125

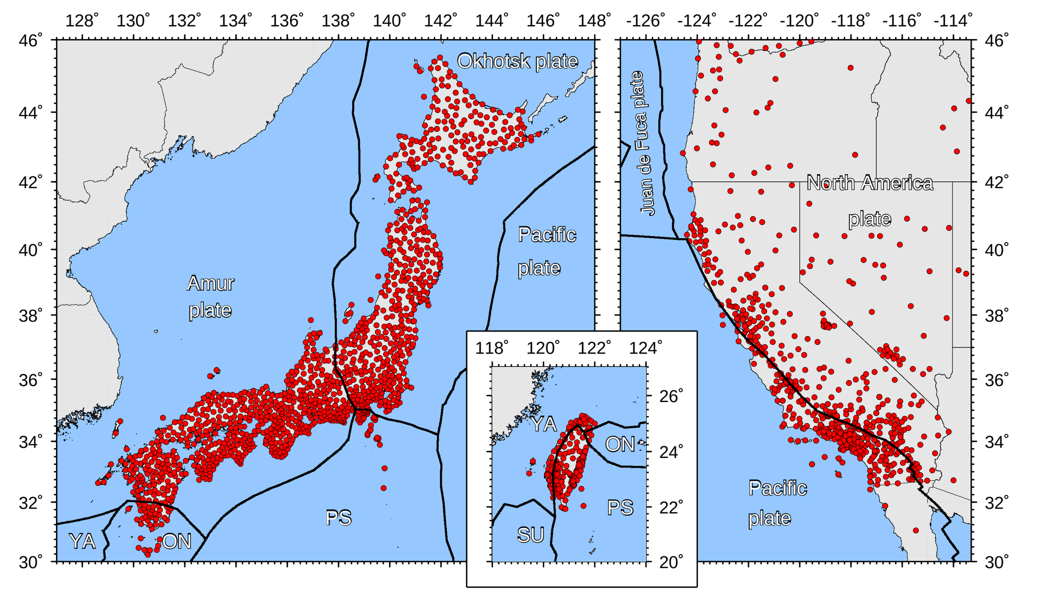

Figure 1: Continuously recording GPS station coverage in Japan, Taiwan, and California. Maps are plotted at the same scale.

1 Overview

The primary objective of this methodological study is to present a wavelet-based multiscale representation of three-component surface velocities, as a tool to facilitate analysis of geodetic observations from dense GPS networks. The density of continuous GPS observations now available for several regions is exemplified by network distribution in Japan, Taiwan, and California (Figure 1).

In comparison to previous GPS studies (e.g., *Feigl et al.*, 1990; *Ward*, 1998; *Beavan and Haines*, 2001), novel aspects of our approach include:

1. an explicit and consistent decomposition of the velocity field into multiple scales at all locations;
2. a minimum scale at which we estimate the velocity field at a particular location that is controlled by the local station coverage;
3. inclusion of the vertical velocity observations if they are available;
4. use of spherical wavelets in representing the velocity field.

2 Multiscale estimation procedure

From a data set of irregularly distributed discrete observations, we seek to estimate a continuous, spatially varying velocity field

$$\mathbf{v}(\theta,\phi) \;=\; v_r(\theta,\phi)\,\hat{\mathbf{r}} \;+\; v_\theta(\theta,\phi)\,\hat{\boldsymbol{\theta}} \;+\; v_\phi(\theta,\phi)\,\hat{\boldsymbol{\phi}},$$

where $\hat{\mathbf{r}}$ is the vertical direction, $\hat{\boldsymbol{\theta}}$ is the south direction, and $\hat{\boldsymbol{\phi}}$ is the east direction.

A scalar function on the surface of the sphere, $d(\mathbf{x})$, — for example, the vertical component of velocity — can be expressed in terms of basis functions, $g_j(\theta,\phi)$, as

$$\hat{d}(\mathbf{x}) \;=\; \sum_{k=1}^{M} m_k\, g_k(\mathbf{x}) \quad\longrightarrow\quad \mathbf{d} = \mathbf{G}\,\mathbf{m}\,.$$

Our choice of basis functions is the "Difference of Gaussian" spherical wavelets of *Bogdanova et al.* (2005) (Figure 2). The solution to the least-squares problem is

$$\mathbf{m} = \left(\mathbf{G}^T\mathbf{C}_{\mathrm{D}}^{-1}\mathbf{G} + \lambda^2\mathbf{S}\right)^{-1}\mathbf{G}^T\mathbf{C}_{\mathrm{D}}^{-1}\mathbf{d}\,,$$

where $\mathbf{C}_{\mathrm{D}}$ is the data covariance matrix, $\mathbf{S}$ is the regularization matrix, and λ is the regularization parameter, which we choose via leave-one-out cross-validation.

Once we have estimated the velocity field $\mathbf{v}(\theta,\phi)$, we can readily compute its surface derivatives and other scalar quantities, like dilatation rate, strain rate and rotation rate. The spatial velocity gradient, $\mathbf{L}$, is defined by

$$\mathbf{L} \;\equiv\; (\boldsymbol{\nabla}\mathbf{v})^T \;=\; \mathbf{v}\boldsymbol{\nabla},$$

and can be decomposed as $\mathbf{L} = \mathbf{D} + \mathbf{W}$, into a symmetric tensor, $\mathbf{D}$, and anti-symmetric tensor, $\mathbf{W}$, as shown next.

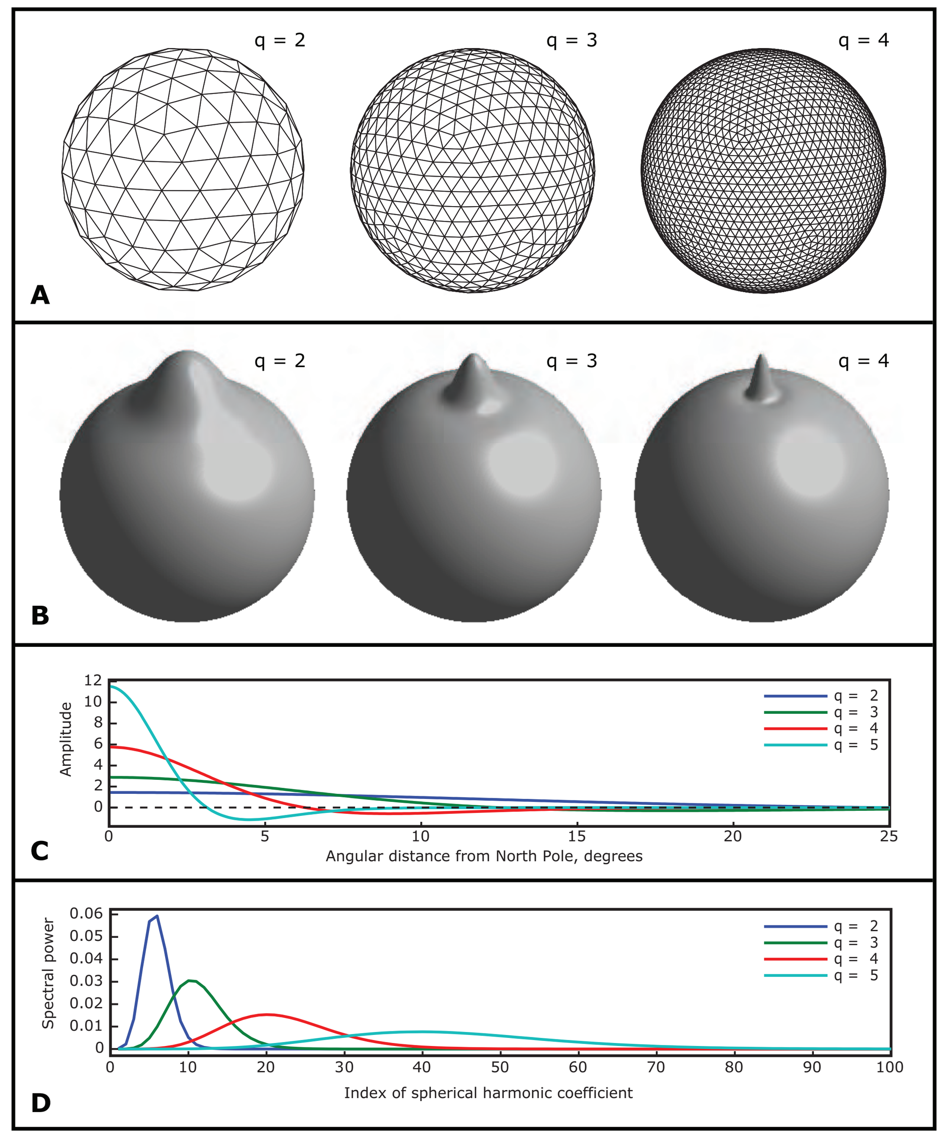

Figure 2: Spherical wavelet frame functions. (a) Spherical grids used for determining the locations for the centers of the spherical wavelet frame functions. (b) Three different scales of a DOG (Difference of Gaussian) spherical wavelets. (c) Longitudinal profiles of wavelets in (b). (d) Harmonic spectra of wavelets in (b).

For a 3D velocity field, the strain-rate and rotation-rate tensors are

$$\mathbf{D} = \begin{bmatrix} \frac{\partial v_r}{\partial r} & \frac{1}{2r}\left(-v_\theta + \frac{\partial v_r}{\partial\theta} + r\frac{\partial v_\theta}{\partial r}\right) & \frac{1}{2r}\left(-v_\phi + \frac{1}{\sin\theta}\frac{\partial v_r}{\partial\phi} + r\frac{\partial v_\phi}{\partial r}\right) \\ D_{12} & \frac{1}{r}\left(v_r + \frac{\partial v_\theta}{\partial\theta}\right) & \frac{1}{2r}\left(-v_\phi\cot\theta + \frac{1}{\sin\theta}\frac{\partial v_\theta}{\partial\phi} + \frac{\partial v_\phi}{\partial\theta}\right) \\ D_{13} & D_{23} & \frac{1}{r}\left(v_r + v_\theta\cot\theta + \frac{1}{\sin\theta}\frac{\partial v_\phi}{\partial\phi}\right) \end{bmatrix}$$

$$\mathbf{W} = \begin{bmatrix} 0 & \frac{1}{2r}\left(-v_\theta + \frac{\partial v_r}{\partial\theta} - r\frac{\partial v_\theta}{\partial r}\right) & \frac{1}{2r}\left(-v_\phi + \frac{1}{\sin\theta}\frac{\partial v_r}{\partial\phi} - r\frac{\partial v_\phi}{\partial r}\right) \\ -W_{12} & 0 & \frac{1}{2r}\left(-v_\phi\cot\theta + \frac{1}{\sin\theta}\frac{\partial v_\theta}{\partial\phi} - \frac{\partial v_\phi}{\partial\theta}\right) \\ -W_{13} & -W_{23} & 0 \end{bmatrix}$$

3 Applications to synthetic and real datasets

We first illustrate the procedure using a velocity field for an infinite strike-slip fault (Figure 3).

Next we use the velocity field from the continuous GPS network in southern California (Figure 4), which contains the vertical component as well. If the velocity field is dominated by net rotation, we remove a uniform rotational field (Figure 5); this represents the longest-scale features of the field. We then estimate the three-component velocity field, $\mathbf{v}(\theta,\phi)$, using spherical wavelets. Equipped with $\mathbf{v}(\theta,\phi)$, we compute the overall dilation-rate, strain-rate, and rotation-rate fields (Figure 6), and also the multiscale components (Figures 7 and 8).

In Figure 9 we present a synthetic example of two dilatational sources with different locations, magnitudes, and signs. Figure 10 shows how the multiscale representation easily captures the two signals in the input velocity field.

4 Toward multiscale time-dependent event detection

Our ultimate objective is to monitor time-dependent signals in dense GPS networks. In this study we have only dealt with the spatial part of the problem, showing that the multiscale representation is well-suited to identifying and characterizing geophysical signals of all scales. This approach is a step toward global multiscale monitoring of time-dependent GPS displacement fields, in hopes of efficient and accurate characterization of Earth's surface deformation and the detection of geophysically interesting phenomena.

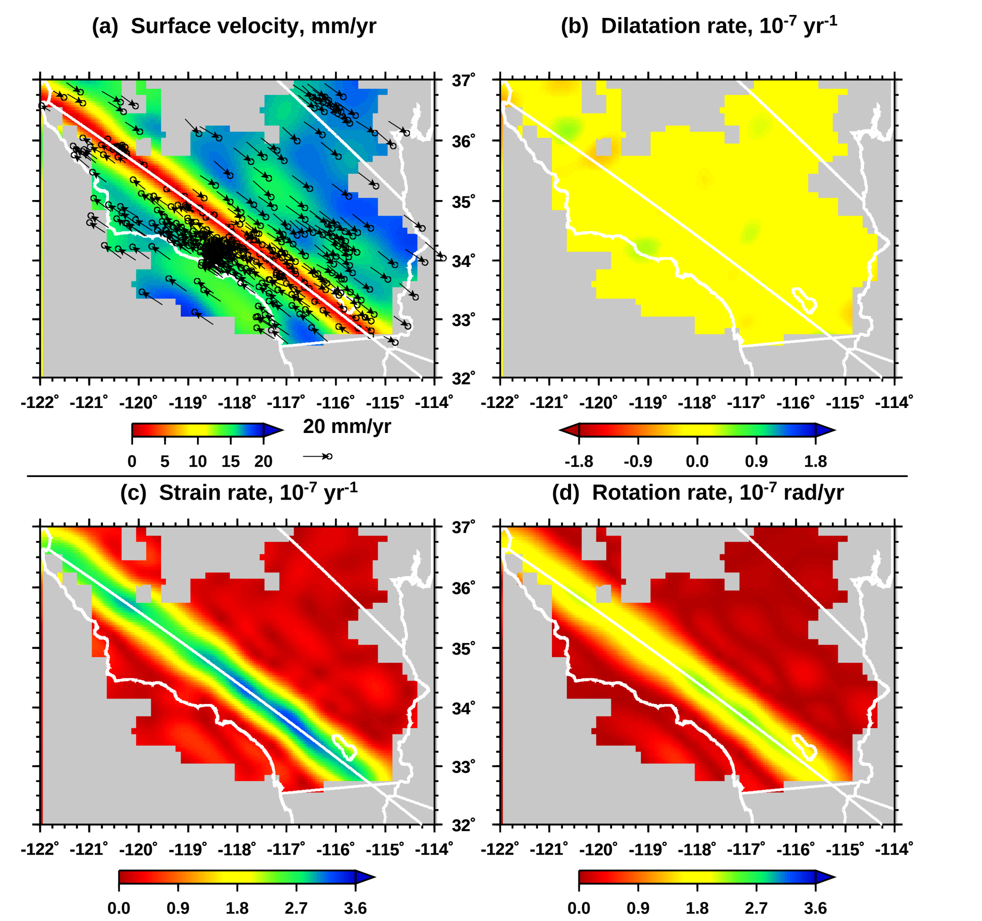

Figure 3: Synthetic example: Interseismic field for a locked strike-slip fault, locked at 15 km depth and slipping at 35 mm/yr. (a) Black arrows denote a synthetic horizontal velocity field with Gaussian errors added, computed at the actual GPS observation points. Background color is the magnitude of the multiscale estimated horizontal velocity field, using scales q=3 to q=7. The q=7 spherical wavelet has a support of 87 km. Dilatation rate (b), strain rate (c), and rotation rate (d), each computed from the estimated velocity field. As expected, the dilatation rate is nearly zero everywhere, while the strain rate is highest near the fault. The mask is applied to regions that are not resolved by the estimated field.

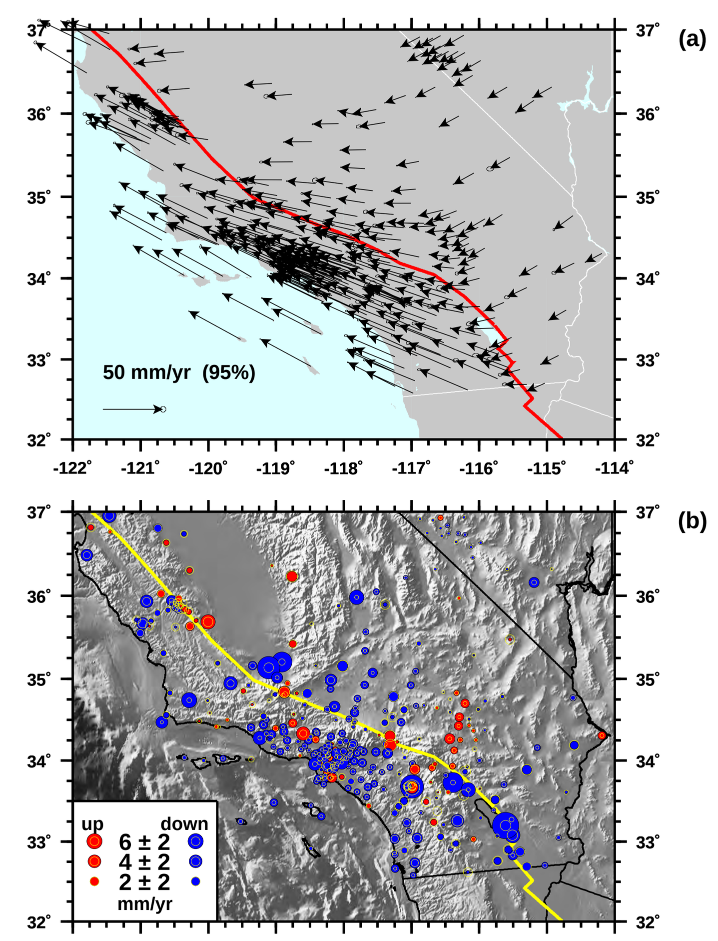

Figure 4: REASoN continuous GPS velocity field, southern California. **(a)** Horizontal component, with ellipses denoting the 95% confidence interval. **(b)** Vertical component, with yellow circles denoting the estimated standard deviation.

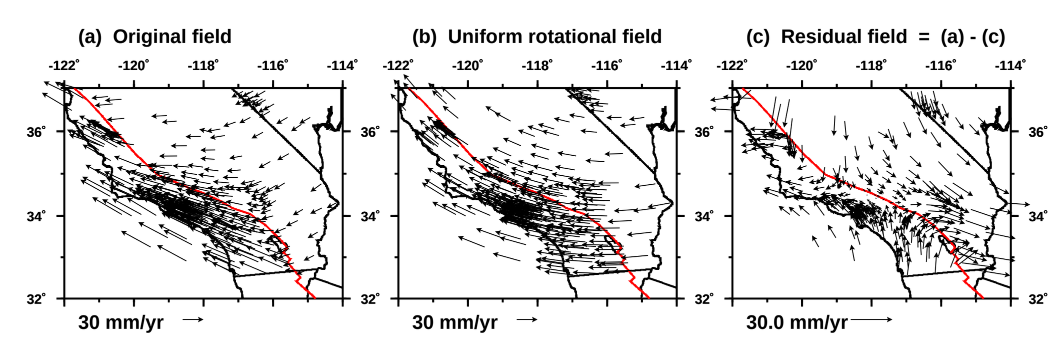

Figure 5: Removing a pure rotational field from the REASoN velocity field. (a) REASoN horizontal velocity field in southern California (Figure 4). (b) Rotational field computed from an estimated Euler vector for the field in (a). (c) Residual field, (a) - (c). The removal of a rotational field has no effect on strain rate and dilatation rate.

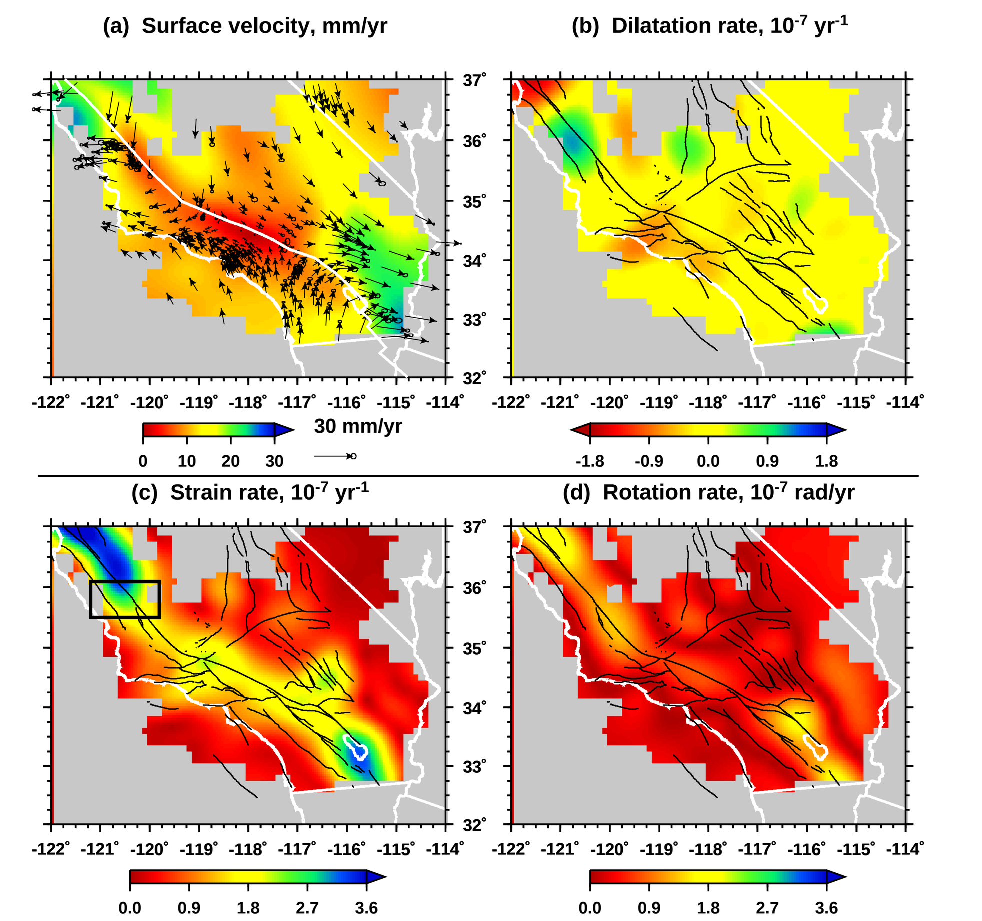

Figure 6: REASoN velocity field. See Figure 3 caption for details. The highest strain rates occur in the regions of Parkfield and the Salton trough.

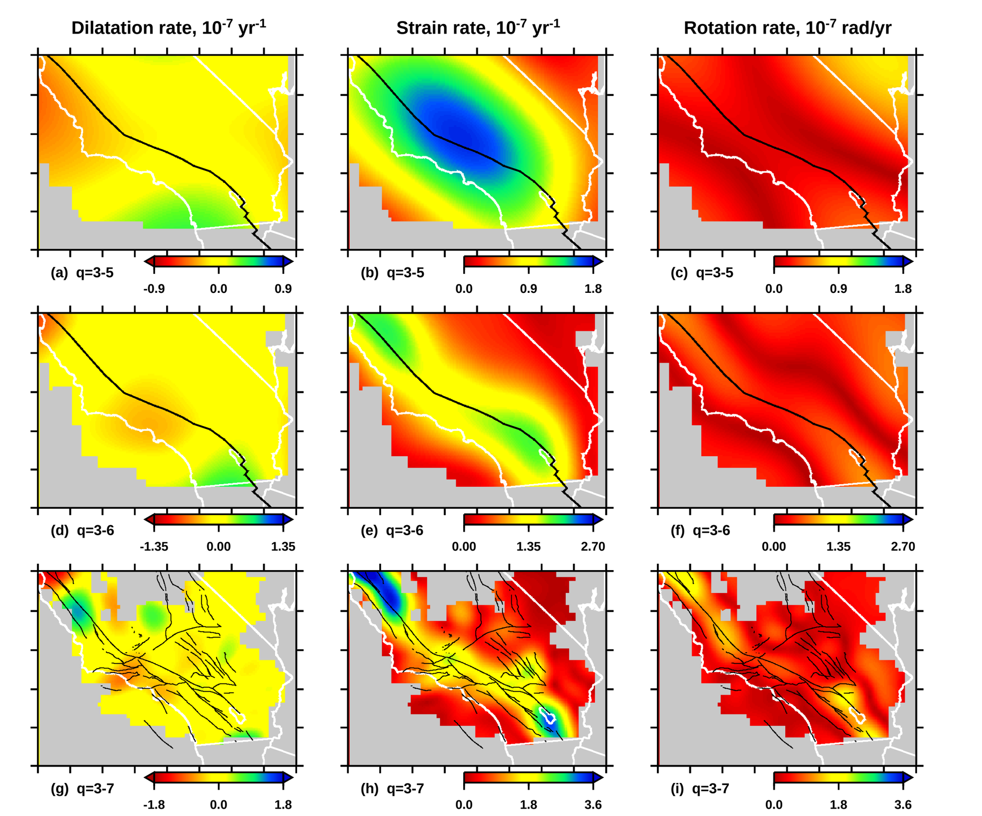

Figure 7: Multiscale estimation of REASoN velocity field in southern California. In each row, from top to bottom, we add an additional finer scale of frame functions in the estimation of the velocity field.

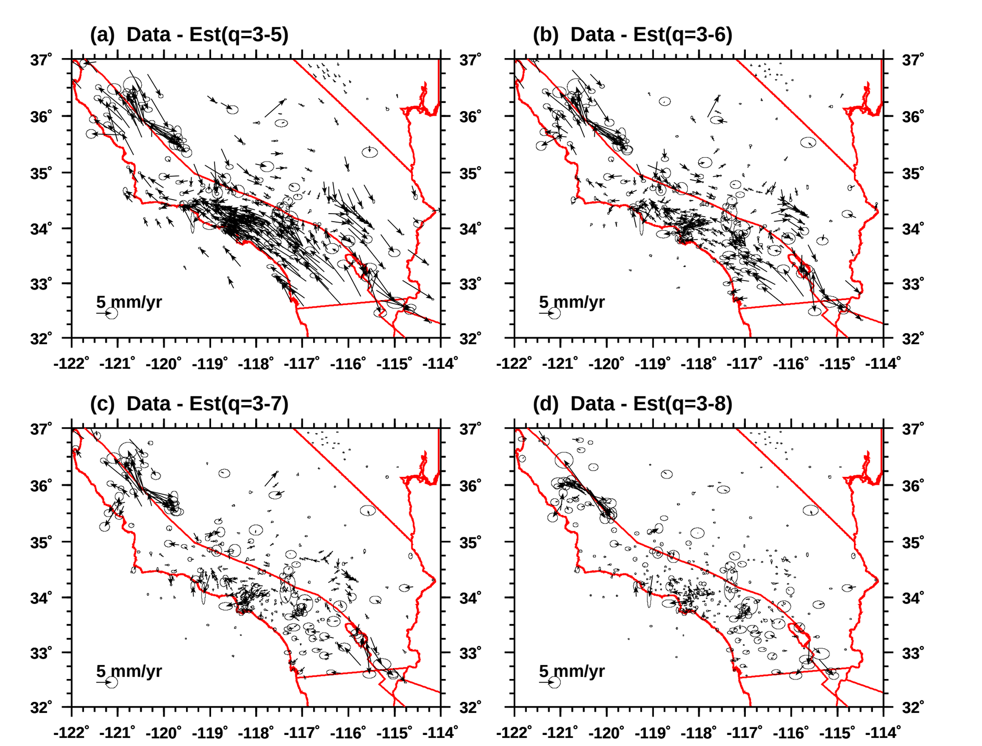

Figure 8: Residual horizontal velocity fields for the REASoN dataset. As shorter scalelengths are included in the estimated field, the residuals decrease.

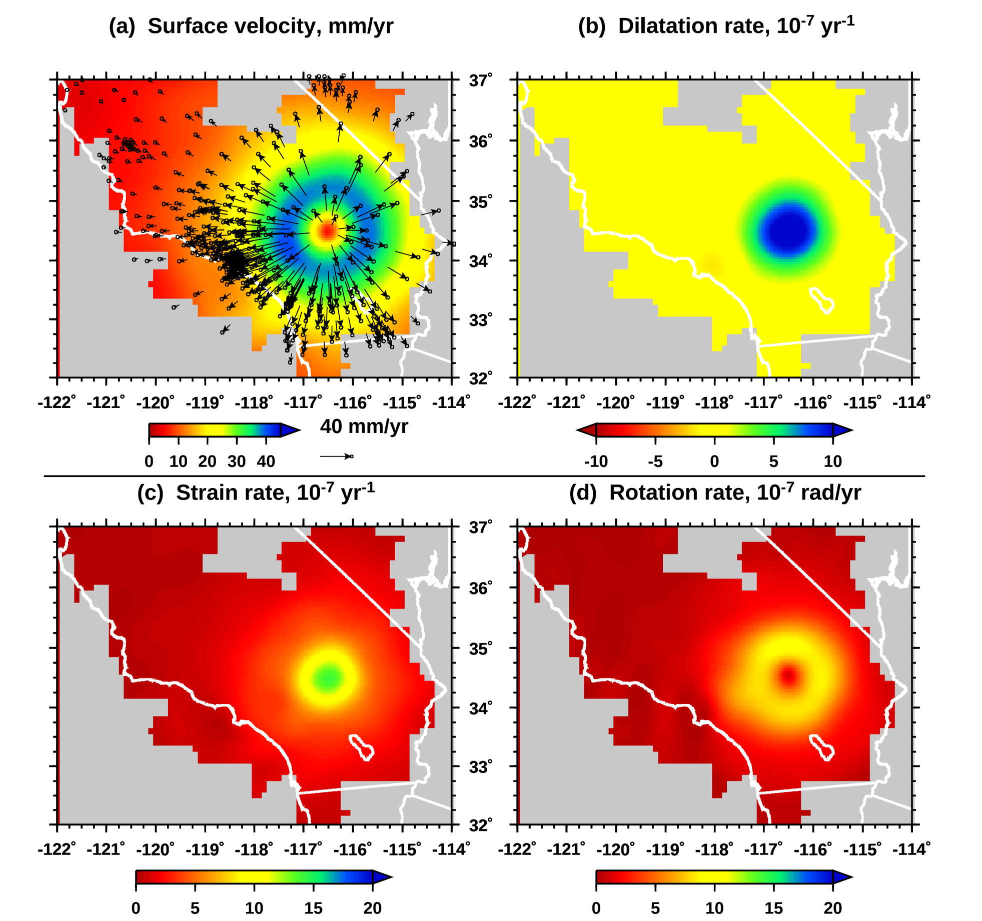

Figure 9: Synthetic example: Two dilatational sources. See Figure 3 caption for details. The tilt due to the vertical field gives rise to the ring-like pattern in the rotational field (d).

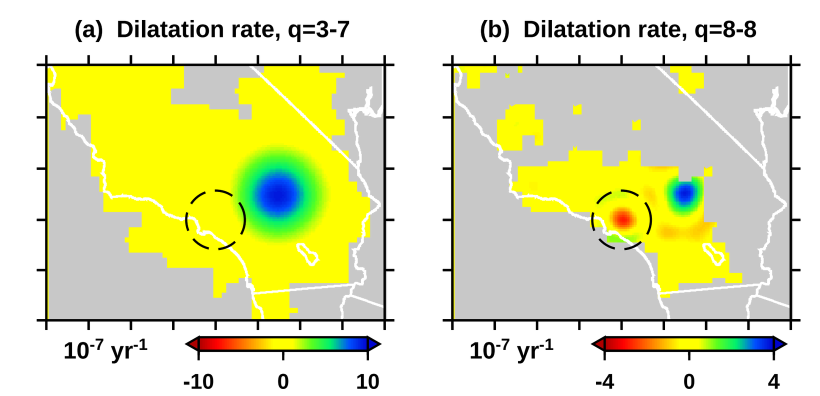

Figure 10: Multiscale estimation of the dilatational field for the synthetic velocity field shown in Figure 9a. Dashed circle corresponds to the region of the smaller, negative dilatational source, which is only apparent at scale scale q=8.

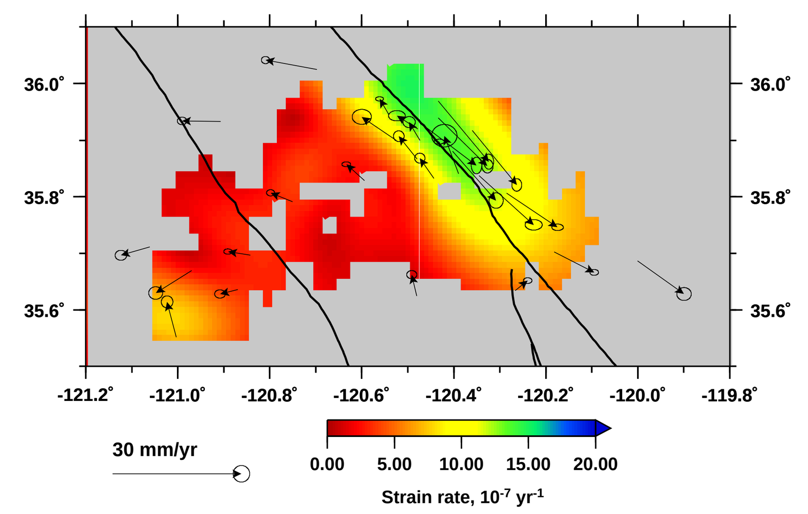

Figure 11: Strain-rate field derived from the multiscale estimation of the REASoN velocity field in the Parkfield region, using only scales q=6 to q=9. In regions of dense station coverage, we are able to compute high strain-rate estimates, if they are present. Here the estimated strain rate across the San Andreas fault is about 1.5×10^{-6} yr^{-1}. See Figure 6c for context.

5 Acknowledgments

We acknowledge the Southern California Integrated GPS Network and its sponsors, the W.M. Keck Foundation, NASA, NSF, USGS, SCEC, for providing data used in this study.

References

NASA REASoN Project, SCIGN Data Portal, http://reason.scign.org/scignDataPortal/.

Beavan, J., and J. Haines, Contemporary horizontal velocity and strain rate fields of the Pacific-Australian plate boundary zone through New Zealand, *J. Geophys. Res.*, *106*(B1), 741–770, 2001.

Bogdanova, I., P. Vandergheynst, J. R. Antoine, L. Jacques, and M. Morvidone, Stereographic wavelet frames on the sphere, *Applied Comput. Harmonic Anal.*, *19*(2), 223–252, 2005.

Feigl, K. L., R. W. King, and T. H. Jordan, Geodetic measurement of tectonic deformation in the Santa Maria fold and thrust belt, California, *J. Geophys. Res.*, *95*(B3), 2679–2699, 1990.

Ward, S. N., On the consistency of earthquake moment rates, geological fault data, and space geodetic strain: the United States, *Geophys. J. Int.*, *134*, 172–186, 1998.